Study of local structure at crystalline rubrene grain boundaries via scanning transmission X-ray microscopy

Alexandre L. Foggiatto[a], Yasuo Takeichi[b,c], Kanta Ono[b,c], Hiroki Suga[d], Yoshio Takahashi[e], Michael A. Fusella[f], Jordan T. Dull[f], Barry P. Rand[f,g], Kentaro Kutsukake[h], Takeaki Sakurai[a]

[a] *Department of Applied Physics, Faculty of Pure and Applied Sciences, University of Tsukuba, Tsukuba, Ibaraki 305-8573, Japan*
[b] *Institute of Materials Structure Science, High-Energy Accelerator Research Organization, Tsukuba, Ibaraki 305-0801, Japan*
[c] *Department of Materials Structure Science, SOKENDAI (The Graduate University for Advanced Studies), Tsukuba, Ibaraki, 305-0801, Japan*
[d] *Department of Earth and Planetary Systems Science, Hiroshima University, Kagamiyama, Higashi-Hiroshima, Hiroshima 739-8526, Japan*
[e] *Department of Earth and Planetary Science, Graduate School of Science, The University of Tokyo, Bunkyo, Tokyo 113-0033, Japan*
[f] *Department of Electrical Engineering, Princeton University, Princeton, New Jersey 08544, United States*
[g] *Andlinger Center for Energy and the Environment, Princeton University, Princeton, New Jersey 08544, United States*
[h] *Institutes of Innovation for Future Society, Nagoya University, Nagoya, Aichi 464-8601, Japan*

Abstract

Rubrene is a promising and archetypal organic semiconductor owing to its high reported hole mobility. However, this high mobility only exists in its crystalline state, with orders of magnitude reduction in disordered films. Thus, as it pertains to thin film polycrystalline rubrene, it is important to understand structure and the presence of disordered regions at grain boundaries. Here, we use scanning transmission X-ray microscopy (STXM) to investigate polycrystalline rubrene thin films with either platelet or spherulite morphology. The STXM images allow us to distinguish and quantify the arrangement of the local structure in the crystal. The analysis suggests that the platelet film has more oriented molecules in the crystal than in the spherulite phase. Also, at spherulite grain boundaries, we reveal a high number of misaligned molecules

Email address: alexandrelfgt@hotmail.com (Alexandre L. Foggiatto)

compared to the smooth boundary in the platelet case, with grain boundary sinuosity of 0.045 ± 0.002 and 0.139 ± 0.002 μm for the platelet and spherulite cases, respectively, which help to explain the higher mobility in the former case.
Keywords: Rubrene, organic semiconductor, X-ray microscope, image analysis
2010 MSC: 00-01, 99-00

1. Introduction

Organic semiconductors have been extensively studied for devices such as field-effect transistors [1], photovoltaic cells [2, 3], and light-emitting diodes [4] due to their promise of low-cost, low temperature, and large area processing. However, organic thin-films used in these devices are usually quite disordered, normally to allow for film uniformity, but which negatively impacts charge transport [5]. The enhancement of carrier mobility in organic semiconductors in recent years has been achieved by improving thin-film crystal quality [6], synthesis of new materials [7], and device engineering [8, 9]. Usually, it is assumed that the major feature that limits carrier mobility in polycrystalline films are grain boundaries, acting as energy barriers or trap sites [10, 11, 12]. However, Vladimirov et al. [13] recently reported that the charge carrier mobility could be restrained by the misalignment of molecules at the grain boundary. Also, Wong et al. observed that TIPS-pentacene grain boundary regions are composed of a random packing of nanocrystallites that could reduce charge carrier mobility [14]. Therefore, continuing to build a comprehensive understanding of the structure and role of grain boundaries is critical for further improvements to organic electronic devices, therefore the analysis of the local structure in this region is of utmost importance.

Rubrene is an archetype organic semiconductor, with demonstrated hole mobility of up to 20 $\mathrm{cm^2V^{-1}s^{-1}}$ in a single crystal [15, 16]. And although as-deposited rubrene thin films are typically amorphous, three distinct crystal phases are known to exist: monoclinic, orthorhombic and triclinic [17, 18]. Of these crystal structures, the orthorhombic phase is of principal interest as it has

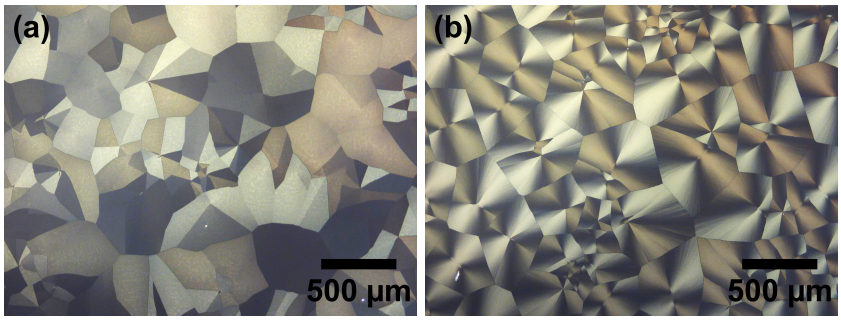

Figure 1: Polarized optical microscope images of crystalline rubrene with (a) platelet and (b) spherulite morphology

demonstrated the highest charge carrier mobility [19]. Many techniques have been developed to obtain crystalline orthorhombic rubrene [18, 20, 21]. Fusella et al. [22] reported that by controlling the annealing temperature of rubrene thermally evaporated on a suitable underlayer, orthorhombic single crystal domains with dimensions on the order of 100 μm can be achieved. Also, it was found that annealing at higher temperatures results in orthorhombic spherulite domains, thus giving the opportunity to investigate grain boundaries in the same material system yet with different morphologies. Polarized optical microscope images of platelet-like single crystal domains and spherulite domains are shown in Fig. 1 (a) and (b), respectively. The primary difference between platelet and spherulite films are that, in the polycrystalline platelet film, each domain is a single crystal orthorhombic grain, whereas in the spherulite film, each domain is not a single crystal, but rather a continuous gradient of rubrene crystals with varying in-plane orientation [23]. We can estimate that the size of the nanocrystals in the spherulite films is on the order of 100 nm, considering the width of the smallest microcrystalline domains.

Such rubrene films have been imaged with polarized optical microscopy and, more recently, electron backscattered diffraction (EBSD) [24]. However, neither EBSD nor optical microscopy have the necessary resolution to resolve grain boundaries in sufficient detail. One technique that is intriguing in this regard is scanning transmission X-ray microscopy (STXM), which, when combined with

near-edge X-ray absorption fine structure (NEXAFS), is effective for identifying and imaging domain structure and orientation with high resolution. Resonance transitions from C 1s to unoccupied π^* and σ^* orbitals can be observed by using soft X-ray energy near the carbon 1s ionization, which allow for determining the orientation of the molecule in the film [25]. Within the STXM experiment, it is possible to select the excitation energy assigned to the transitions observed in the NEXAFS spectrum. By performing a raster scan over the sample for a fixed energy, the absorption of a specific energy as a function of position can be measured. This technique has been successfully used to determine the orientation of organic molecules in numerous systems [26, 27, 28, 29].

In this work, we use STXM combined with image analysis to investigate the local structure of polycrystalline orthorhombic rubrene thin films, either in the form of platelets or spherulites. These films were reported to have hole mobilities of 4 and 1 $cm^2V^{-1}s^{-1}$ for the platelet and spherulite morphologies, respectively [22], thought to be due to the increased density of grain boundaries in the latter. Here, via STXM measurements and analysis, we establish better insight for the mobility differences in these two films through an analysis of morphological differences in the vicinity of grain boundaries which reveals not only are they more frequent, but grain boundaries are also wider and more disordered in spherulite films compared to abrupt grain boundaries in the platelet films.

2. Experimental

The growth and STXM imaging were performed on X-ray transparent silicon nitride membranes. Optical microscope images of the films on the SiN membranes are shown in Fig. A.7). 40 nm of rubrene (Nichem, purified by thermal gradient sublimation) atop a 6 nm thick film of TPTPA (tris(4-(5-phenylthiophen-2-yl)phenyl)amine, Lumtec, used as received) were deposited by thermal evaporation in a vacuum chamber with base pressure $\sim 10^{-7}$ Torr. TPTPA was used as an underlayer to assist the crystallization as described

previously [22]. Crystallization was achieved by annealing the samples on a preheated hot plate in a nitrogen glovebox. The platelet samples were annealed at 140 ℃ for 5 min, and the spherulite samples were annealed at 170 ℃ for 30 - 45 s.

The morphology was investigated using the compact STXM at BL-13A of the Photon Factory, KEK [30]. Molecular orientation was evaluated by switching in-plane horizontal and vertical linear polarization of the APPLE-II type undulator radiation. The image size was set as 10 μm $\times$ 10 μm and the pixel size was 0.1 μm and 0.05 μm for the platelet and spherulite samples, respectively. The NEXAFS spectra were obtained by averaging the absorption in an image sequence (stack) of scans acquired at the C K-edge (280 - 310 eV). The raw data were converted into images and analyzed using scripts written in Python 3.

3. Results and Discussion

Figure 2 displays NEXAFS spectra of the platelet rubrene film using linearly polarized light. The peaks at 284.2, 285.1 and 285.9 eV have already been assigned as α, β and γ, respectively [31]. These excitation peaks are due to the transition from C 1s to the π^* molecular orbital. The intensity of the α and γ peaks are sensitive to the orientation of the backbone structure, while the β intensity is sensitive to the phenyl side group structure of rubrene [32]. The two broader peaks at 289 and 294 eV are owing to transitions from C 1s to the σ^* molecular orbital. In our experimental set up, the samples were fixed normal to the incident radiation, thus the dipole moment of the tetracene cores and phenyl side groups of rubrene are projected on the plane, allowing us to extract in-plane orientation information. Although out-of-plane information can also be extracted with STXM, prior X-ray and EBSD analysis showed that the rubrene molecules are uniformly aligned out-of-plane [22], and thus here we focus on in-plane orientation. Figure 2 (a) and (b) show NEXAFS spectra for two distinct crystal domains of a platelet film. It can be noted that the resonance inten-

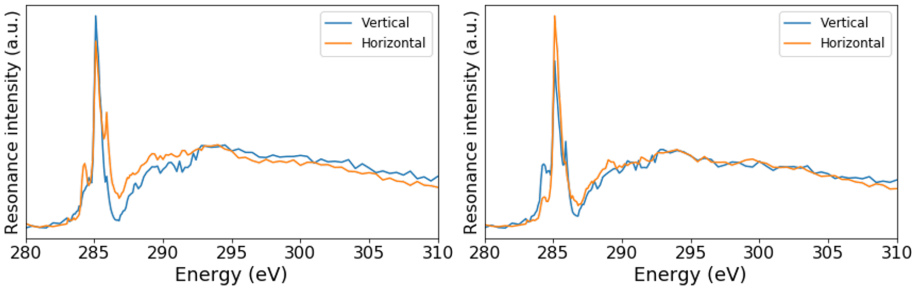

Figure 2: NEXAFS spectra for two distinct regions (i.e. crystal domains) of a rubrene platelet polycrystalline film using in-plane vertical and horizontal polarization. The α, β and γ assigned peaks at 284.2, 285.1 and 285.9 eV correspond to C 1s to π^* molecular orbital transitions. The α, β and γ peaks in each image exhibit a complementary pattern, for the same polarization, which infers that the molecules in these regions have different orientations.

sities for these two distinct regions are different, denoting different molecular orientations.

Figure 3 displays raw STXM images of a rubrene spherulite film taken at various photon energies. The color contrast reflects the NEXAFS spectral intensity (cf. Fig. 2). In the images taken at 284.2 (Fig. 3 (a) and (d)) and 285.9 eV (Fig. 3 (c) and (f)) the complementary contrast under different polarization can be clearly distinguished. The uniform color contrast of each grain suggests a crystal domain. However, for the image taken at 285.1 eV (Fig. 3 (b) and (e)), contrast is minimal. This is likely due to the fact that the large resonance peak at 285.1 eV overlaps with the other two, shadowing the image [32]. This is the same effect that turns the images taken at 285.9 eV darker than the one taken at 284.2 eV. To minimize the computational error and to obtain more precise information, our analysis focuses on the α peak energy (284.2 eV). Finally, as a control, Fig. 3(g) displays the pre-edge image, taken at 283.8 eV. No pattern is observed in this image, consistent with our discussion.

Performing STXM image analysis allows us to derive a better understanding of the local structure of rubrene thin films by extracting numerical parameters that help us elucidate orientational and morphological differences. Figure 4 (a)

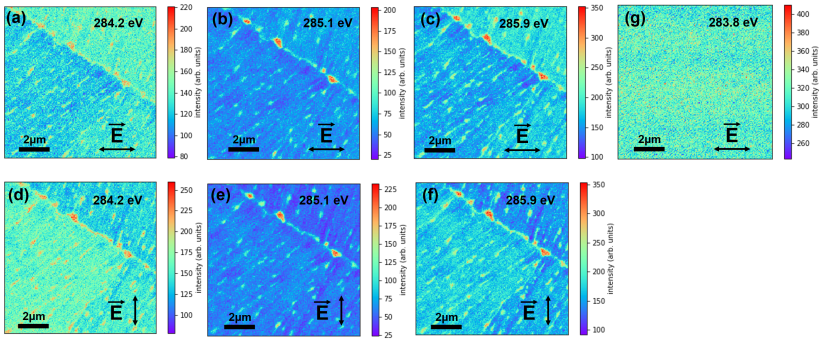

Figure 3: 10 μm $\times$ 10 μm unprocessed STXM images for a spherulite rubrene film taken at 284.2, 285.1 and 285.9 eV, using (a-c) in-plane horizontally and (d-f) vertically polarized light. (g) The pre-edge was taken at 283.8 eV using horizontally polarized light.

and (b) display maps of the optical density (OD) at each point for the platelet and spherulite films, respectively. The OD is defined as $\ln(I/I_0)$, where I is the transmitted intensity and I_0 is the background normalized to the pre-edge. The platelet film exhibits two uniform grains, while the spherulite sample has micro-domains within a large domain and a rougher, more poorly defined, domain boundary. Since the films were prepared at temperatures below TPTPA crystallization temperature, we can assume that the difference in the OD images emerge solely from rubrene. Using the normalized and aligned OD data, the in-plane molecular orientation map can be obtained from the following equation [28]:

$$OD = M(P\cos^2(\beta+\theta) + (1-P)\sin^2(\beta+\theta)) + C. \quad (1)$$

where P is the Stöhr polarizer coefficient, M is defined as the magnitude of the in-plane component of the normalized resonance intensity and C is a constant resonance intensity. θ is the in-plane angle of the molecule and β is the in-plane incident angle of the polarized radiation, in which the values of β are defined from the horizontal polarization.

The in-plane molecular orientation map of platelet and spherulite rubrene films are displayed in Fig. 5 (a) and (b), respectively. For each point, θ is ob-

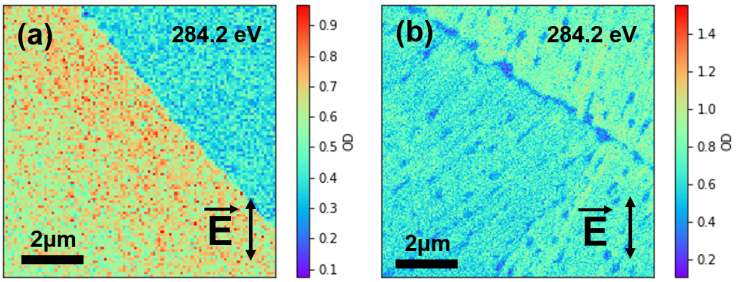

Figure 4: OD transmission image for (a) platelet and (b) spherulite films taken at 284.2 eV using in-plane vertically polarized light.

tained by dividing the horizontal ($\beta = 0$) by the vertical ($\beta = \pi/2$) polarized OD using Eq. 1. To perform the calculation, C was set as 0 and P as 1, resulting in $OD \propto \cos^2(\theta)$. In this case, θ is defined in relation to the polarized radiation. If $\theta = 0$, the dipole moment of molecules are parallel to the horizontal polarized radiation. It can be seen that molecules in the platelet film are more homogeneously oriented within the respective domain compared to the spherulite domain, as would be expected given the considerable growth front nucleation that characterizes spherulite growth. The platelet rubrene thin film (Fig. 5(a)) displays two distinct grains. Despite the grain's homogeneity, we notice a film defect in the upper corner of the grain boundary (Fig. 5(a) inset), however the resolution is not high enough to determine the origin of the defect. In Fig. 5(b), on the other hand, the spherulite film grain boundary is less abrupt due to the line patterns (intradomain grain boundaries) that are characteristic of the spherulite morphology. Here, intradomain grain boundary is defined as the boundary between the growth rays created by the non-perfect alignment of molecules in the crystal due to rapid crystallization. It is possible to observe the periodicity of them inside the grain. Although the resolution is not enough to resolve them, we can estimate the width of the smallest microdomains as 100 nm, which can be associated with the size of the nanocrystals. Although these intradomain boundaries, in general, have the same preferential direction inside

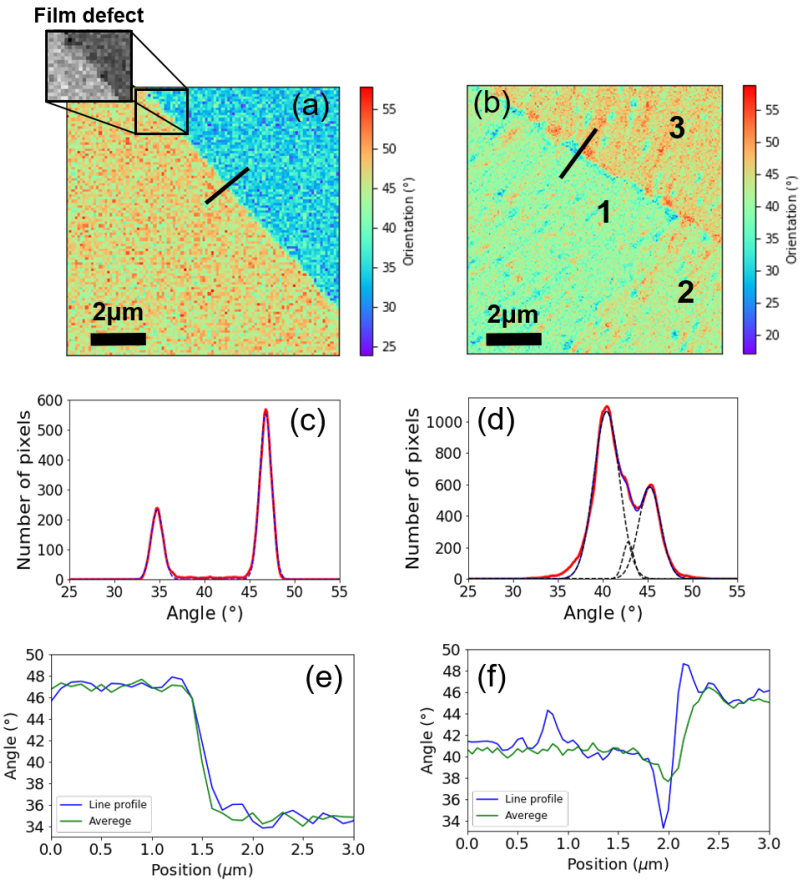

Figure 5: Angular orientation maps for (a) platelet and (b) spherulite films. The inset in (a) displays a high contrast image of the grain boundary in which defects in the film can be seen as black dots. The numbers 1 to 3, in (b), label the three regions referenced in the text. Histograms for (c) platelet and (d) spherulite films. The dashed line corresponds to a Gaussian fit. The line profiles in (a) and (b) are displayed in (e) and (f), respectively. The green line is the average of the line profile taken over the entire length of the grain boundary.

the grain, towards the nucleation center, the rays are not completely parallel to each other. This feature is responsible for the unclear boundary in the 1-2 region of Fig. 5(b). On the contrary, the 1-3 grain boundary is well defined, because it is formed by the encounter of rays from two different nucleation centers. In contrast, the grain boundary in the 1-2 region originates from the same

nucleation center (A.8 (b)).

Here, two regions of 100 μm^2 around the grain boundary are selected for analysis, which contain two (platelet sample) and three (spherulite sample) grains. Prior to the selection of an area, others samples and regions were investigated using a larger field of view (i.e. pixel size) to define the region of interest, as displayed in Fig. A.8. The spherulite film presents micro-domains that extend from the nucleation center throughout the grain and the boundaries are more sinuous than the one in the platelet sample. Also, the platelet film presents no micro-domain, which is expected in a single crystal. Thus, although the selected area is small in comparison to the film size, no substantial deviation from what is observed here is expected if other regions were selected.

To investigate the molecular orientation distribution, shown in Fig. 5 (c) and (d) are histograms of the in-plane orientation maps of the platelet and spherulite films, respectively. The noise was reduced by using a median filter on both images. The histogram for the platelet rubrene film displays two well-defined peaks. In contrast, the angular distribution for the spherulite film portrays a more spread distribution, which corresponds to a less ordered film. Fitting a Gaussian function to the histograms, we could obtain the full width at half maximum (FWHM) for each sample. The platelet film histogram is fitted by two Gaussians centered at 34.77° and 46.83°, and the angular distribution has FWHM = 1.12° for both grains. The spherulite thin film histogram, on the other hand, cannot be fit by two Gaussian functions. Instead, three are needed, centered at 40.45°, 42.88° and 45.26°, with the 42.88° sourcing from region 2 (Fig. 5(b)). The FWHM are 2.38° and 2.03° for the lower and higher angle, respectively. The broadening of the angular distribution is a useful way to quantify the grain disorder, which means that the platelet film has a more uniform orientation and fewer misaligned molecules than the spherulite film. We can also observe a tailing on the borders of the spherulite film histogram (Fig. 5(d)) that cannot be fitted by Gaussian distribution, which indicate a higher number of disordered molecules.

Figure 5 (e) and (f) (blue curves) display line profiles at the grain boundaries.

The platelet thin film exhibits a smoother molecular in-plane orientation than the spherulite one, and the transition between domains is abrupt comparing the former to the latter. In addition, within the domain, the line profile of the spherulite sample displays a molecular mismatch at the boundary. The electrostatic interaction between neighboring molecules and the molecules in the adjacent crystal affects the orientation of molecules in the grain boundary resulting in the misaligned region. To extract information over more of the grain boundary, the angular distribution was averaged along the grain boundary length and plotted as a function of position, as shown in Fig. 5 (e) and (f) (green curves). It can be noticed that the misaligned molecules at the grain boundary in the spherulite film are a common occurrence, and the same feature is not present in the platelet sample. The high number of misaligned molecules at the boundary of the spherulite film indicated in the line profile make up the populations in the tails of the histograms in Fig. 5(d).

By observing the difference of the averaged region and the line profile, one can notice that the center of the grain boundary deflects more from its initial position in the spherulite sample (Fig. 5(f)) compared to the platelet one (Fig. 5(e)). This means that the grain border in the spherulite film is more sinuous. In order to investigate and quantify it, we calculate the root mean square (RMS) for the center of the boundary to define sinuosity on the boundary. First, to identify the center of the boundary (x_0), we calculate the position of the medium point between the two domain plateaus by fitting the line profile using a step function that resembles its shape and extract its value. Thus, the curve is fitted by a sigmoid function:

$$f(x) = a + \frac{b}{1 + e^{\lambda(x - x_0)}}, \tag{2}$$

where x is position. The value for x_0 can be found by adjusting the parameters a, b and λ (supplementary A.9). Then, the same process was repeated over the length of the grain boundary. To minimize error, the line profile was averaged over every three pixels and the result was fitted by a sigmoid function (Eq. 2). Subsequently, Fig. 6 (a) and (b) display x_0 plotted over the grain

boundary of the platelet and spherulite sample, respectively. In order to easily display the results, in Fig. 6 (a) and (b), the grain boundary regions were rotated 48.80° and 33.26°, respectively, to be parallel to the horizontal axis. The good agreement between the calculated border line and the image confirms the accuracy of this process. After defining the boundary position, the RMS can be computed as 0.045 ± 0.002 and 0.139 ± 0.002 μm for the platelet and spherulite films, respectively. The uncertainty in the RMS was obtained by fitting the grain boundary region 200 times. In each cycle, a small variation was inserted in the initial pre-optimized fitting parameters. Consequently, the uncertainty is given by the standard variation of the mean value of the result. The result demonstrates that the molecules at the interface are not only orientationally misaligned at the grain boundary, but also the border is not straight. The high RMS value for the spherulite film is due to the independent growth of the rays from the nucleation center. They are not limited in the boundary by the adjacent rays. On the order hand, in the platelet film, the absence of rays allows the formation of a straight border line. More information about how RMS values were calculated is described in Appendix A.3.

We have also analyzed a 1 μm region on either side of the grain boundary. As displayed in Supplementary A.9, we can integrate the mismatched orientation angle in the vicinity of the grain boundary, which indicates numerically the molecular disorder. The histogram for the spherulite grain border region (Fig. 6(c)), as expected, resembles the full one (Fig. 5(d)). And, the two peaks centered at 39.41° and 45.72°, have a broad angular distribution with the FWHM calculated as 3.80° and 2.20°, respectively. This indicates that the misaligned molecules are more localized at the grain boundary than the inner part of the grain. Since the analyzed region contains the same amount of material, the area under the curve should be similar for both peaks. Indeed, the area under the curves are calculated as 210.74 and 197.79, a difference of approximately 6%. Also in Fig. 6(c), the tailing is more prominent, which agrees with our discussion that the broadening of the histogram and the tailing for low and high angles are associated with the misaligned molecules observed in the line profile (Fig. 5(f)).

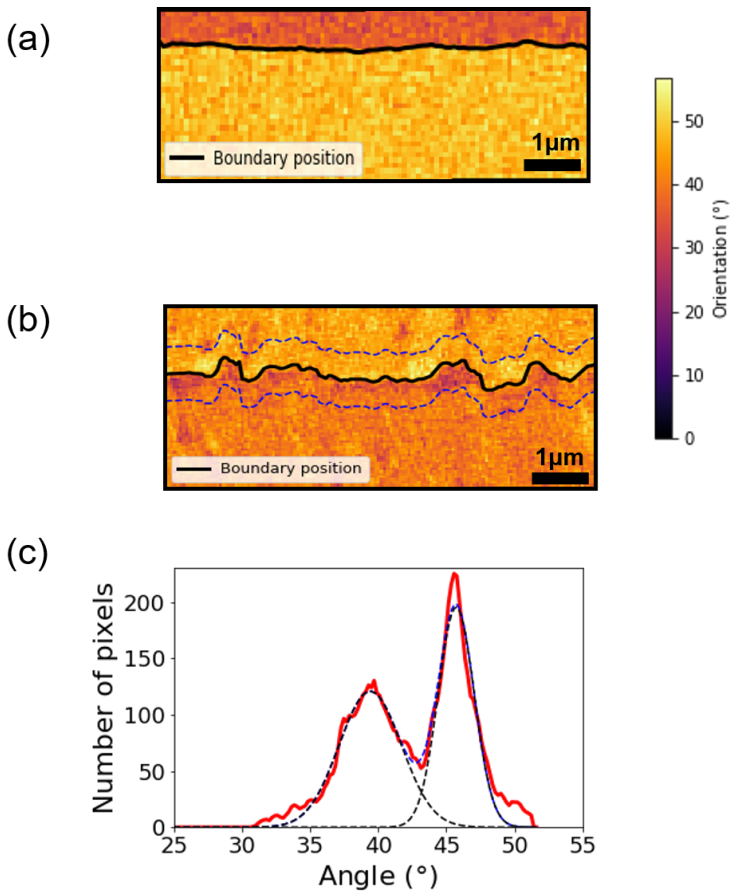

Figure 6: A grain boundary region for (a) platelet and (b) spherulite rubrene films. The black line corresponds to the x_0 calculated using Eq. 2 to fit the center of the grain boundary. The grain boundary is displayed aligned to the horizontal. The blue dashed lines in (b) delineate 1 μm around x_0. (c) The histogram (red solid line) and Gaussian fit (blue dashed line) obtained from the 1 μm region around x_0 for the spherulite film. The peaks were fitted with two Gaussians centered at 39.41° and 45.72°, with FWHM of 3.80° and 2.20°, respectively.

The platelet and spherulite morphologies can be achieved by thermal evaporation of rubrene on an appropriate organic underlayer and selecting the correct annealing temperature [22]. The underlayer improves the crystallization of rubrene by assisting the molecules to rotate in order to find a lowest energy position and orientation. However, annealing at high temperature may inhibit

long-range order owing to more energy and more rapid crystallization, generating the spherulite morphology. Although they have the same crystal phase and out-of-plane orientation, the charge carrier mobility of the platelet form has already been reported as 3-4 times higher than the spherulite one [22]. It was suggested that carrier mobility in the platelet morphology is higher due to the absence of intradomain grain boundaries. As observed in the STXM image analysis, it is not only the presence of more grain boundaries, but the grain boundary of the spherulite crystal has a rougher boundary and more misaligned molecules which may also have a role, perhaps dominant, in limiting the charge carrier mobility. To validate this claim, future work should consider electrical transport and photoluminescence imaging measurements at the grain and grain boundary regions.

4. Conclusion

In conclusion, we have examined the local structure in two different types of crystalline rubrene films, those based upon platelet single crystals and spherulites, using STXM image analysis. It was observed by analysis of the molecular angular distribution that the platelet rubrene film has more homogeneously oriented molecules in each grain and an abrupt, well-ordered grain boundary. In contrast, the spherulite film has misaligned molecules at the grain boundary and a roughness of the boundary. We suggest that the misalignment of rubrene molecules at the grain boundary may create scattering or trapping centers that reduce the charge carrier mobility for the spherulite film compared to the platelet one, further highlighting the importance of controlling morphology to optimize charge carrier and exciton transport processes in molecular thin films.

Acknowledgements

A.L.F. acknowledges the Japanese Government for providing financial assistance to conduct this work through Monbukagakusho (MEXT) scholarship. M.A.F, J.T.D., and B.P.R. acknowledge funding from the National Science

Foundation, award no. ECCS-1709222. This work was supported by JSPS Grants-in-Aid for Scientific Research 16K04943 and it was performed under the approval of the Photon Factory Program Advisory Committee (Proposal No. 2016S2-003).

Appendix A. Supplementary information

Appendix A.1. Optical microscope images

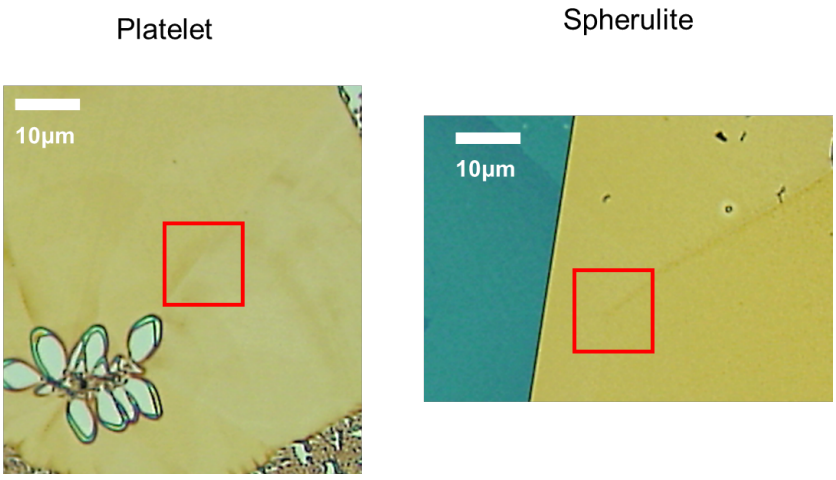

Figure A.7: Optical microscope images of the platelet and spherulite films. The STXM analyzed regions are the ones delimited by the red rectangle.

Appendix A.2. untreated STXM images

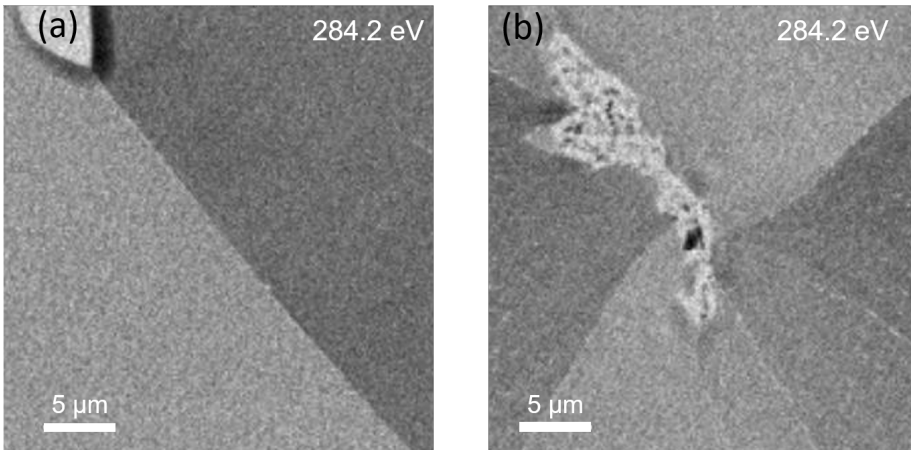

Figure A.8: Untreated data obtained from the STXM of (a) platelet and (b) nucleation center of spherulite films taken at 284.2 eV. The pixel size was set as 0.2 μm.

Appendix A.3. Grain boundary analysis

The RMS values were calculated using the center of the grain boundary extracted by fitting the line profile with a step function (Eq. 2). The fitting is displayed in Fig. A.9. By arranging the center of the grain boundary as a function of the position, the RMS can be calculated. One may have concerns about the validity of this value compared to the resolution of the images. In fact, we used a mathematical approach to obtain the center of the line profile and, since a point has no dimension, the RMS can be smaller than the pixel size. We use a mathematical tool to define more precisely and to study the region around the grain boundary, as displayed in Fig. 6(b), since a substantial difference on the grain boundary sinuosity of the two films is observed.

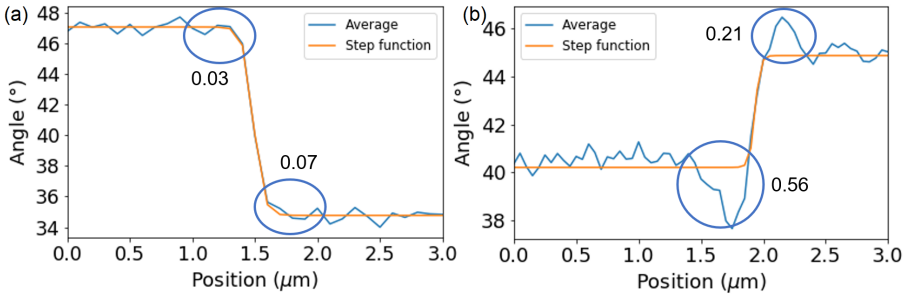

Figure A.9: Step function fitting on the average line profile for (a) platelet and (b) spherulite films. The values displayed in the images correspond to the under/above the fitting curve in the 1 μm around the center of the grain boundary.

References

References

[1] C. Wang, H. Dong, W. Hu, Y. Liu, D. Zhu, Semiconducting π-conjugated systems in field-effect transistors: a material odyssey of organic electronics, Chemical Reviews 112 (4) (2011) 2208–2267 (2011). doi:10.1021/cr100380z.

[2] C. W. Tang, Two-layer organic photovoltaic cell, Applied Physics Letters 48 (2) (1986) 183–185 (1986). doi:10.1063/1.96937.

[3] L. Meng, Y. Zhang, X. Wan, C. Li, X. Zhang, Y. Wang, X. Ke, Z. Xiao, L. Ding, R. Xia, et al., Organic and solution-processed tandem solar cells with 17.3% efficiency, Science 361 (6407) (2018) 1094–1098 (2018). doi:10.1126/science.aat2612.

[4] T.-H. Han, Y. Lee, M.-R. Choi, S.-H. Woo, S.-H. Bae, B. H. Hong, J.-H. Ahn, T.-W. Lee, Extremely efficient flexible organic light-emitting diodes with modified graphene anode, Nature Photonics 6 (2) (2012) 105 (2012). doi:10.1038/NPHOTON.2011.318.

[5] J.-P. Yang, F. Bussolotti, S. Kera, N. Ueno, Origin and role of gap states in organic semiconductor studied by UPS: as the nature of organic molecular crystals, Journal of Physics D: Applied Physics 50 (42) (2017) 423002 (2017). doi:10.1088/1361-6463/aa840f.

[6] K. Nakayama, Y. Hirose, J. Soeda, M. Yoshizumi, T. Uemura, M. Uno, W. Li, M. J. Kang, M. Yamagishi, Y. Okada, et al., Patternable solution-crystallized organic transistors with high charge carrier mobility, Advanced Materials 23 (14) (2011) 1626–1629 (2011). doi:10.1002/adma.201004387.

[7] K. Takimiya, S. Shinamura, I. Osaka, E. Miyazaki, Thienoacene-based organic semiconductors, Advanced Materials 23 (38) (2011) 4347–4370 (2011). doi:10.1002/adma.201102007.

[8] K. Cnops, B. P. Rand, D. Cheyns, B. Verreet, M. A. Empl, P. Heremans, 8.4% efficient fullerene-free organic solar cells exploiting long-range exciton energy transfer, Nature Communications 5 (2014) 3406 (2014). doi:10.1038/ncomms4406.

[9] H. Klauk, Organic thin-film transistors, Chemical Society Reviews 39 (7) (2010) 2643–2666 (2010). doi:10.1039/b909902f.

[10] S. Verlaak, V. Arkhipov, P. Heremans, Modeling of transport in polycrystalline organic semiconductor films, Applied Physics Letters 82 (5) (2003) 745–747 (2003). doi:10.1063/1.1541112.

[11] C. Qian, J. Sun, L. Zhang, H. Huang, J. Yang, Y. Gao, Crystal-domain orientation and boundary in highly ordered organic semiconductor thin film, The Journal of Physical Chemistry C 119 (27) (2015) 14965–14971 (2015). doi:10.1021/acs.jpcc.5b03727.

[12] G. Horowitz, M. E. Hajlaoui, Mobility in polycrystalline oligothiophene field-effect transistors dependent on grain size, Advanced Materials 12 (14) (2000) 1046–1050 (2000). doi:10.1002/1521-4095(200007)12:14<1046::AID-ADMA1046>3.0.CO;2-W.

[13] I. Vladimirov, M. Kühn, T. Geßner, F. May, R. Weitz, Energy barriers at grain boundaries dominate charge carrier transport in an electron-conductive organic semiconductor, Scientific Reports 8 (1) (2018) 14868 (2018). doi:10.1038/s41598-018-33308-y.

[14] C. Y. Wong, B. L. Cotts, H. Wu, N. S. Ginsberg, Exciton dynamics reveal aggregates with intermolecular order at hidden interfaces in solution-cast organic semiconducting films, Nature Communications 6 (2015) 5946 (2015). doi:10.1038/ncomms6946.

[15] V. Podzorov, E. Menard, A. Borissov, V. Kiryukhin, J. Rogers, M. Gershenson, Intrinsic charge transport on the surface of organic semicon-

ductors, Physical Review Letters 93 (8) (2004) 086602 (2004). doi:10.1103/PhysRevLett.93.086602.

[16] Y. Okada, K. Sakai, T. Uemura, Y. Nakazawa, J. Takeya, Charge transport and hall effect in rubrene single-crystal transistors under high pressure, Physical Review B 84 (24) (2011) 245308 (2011). doi:10.1103/PhysRevB.84.245308.

[17] O. D. Jurchescu, A. Meetsma, T. T. Palstra, Low-temperature structure of rubrene single crystals grown by vapor transport, Acta Crystallographica Section B: Structural Science 62 (2) (2006) 330–334 (2006). doi:10.1107/S0108768106003053.

[18] L. Huang, Q. Liao, Q. Shi, H. Fu, J. Ma, J. Yao, Rubrene micro-crystals from solution routes: their crystallography, morphology and optical properties, Journal of Materials Chemistry 20 (1) (2010) 159–166 (2010). doi:10.1039/b914334c.

[19] X. Wang, T. Garcia, S. Monaco, B. Schatschneider, N. Marom, Effect of crystal packing on the excitonic properties of rubrene polymorphs, CrystEngComm 18 (38) (2016) 7353–7362 (2016). doi:10.1039/c6ce00873a.

[20] T. Matsukawa, M. Yoshimura, K. Sasai, M. Uchiyama, M. Yamagishi, Y. Tominari, Y. Takahashi, J. Takeya, Y. Kitaoka, Y. Mori, et al., Growth of thin rubrene single crystals from 1-propanol solvent, Journal of Crystal Growth 312 (2) (2010) 310–313 (2010). doi:10.1016/j.jcrysgro.2009.10.048.

[21] H. M. Lee, H. Moon, H.-S. Kim, Y. N. Kim, S.-M. Choi, S. Yoo, S. O. Cho, Abrupt heating-induced high-quality crystalline rubrene thin films for organic thin-film transistors, Organic Electronics 12 (8) (2011) 1446–1453 (2011). doi:10.1016/j.orgel.2011.05.015.

[22] M. A. Fusella, S. Yang, K. Abbasi, H. H. Choi, Z. Yao, V. Podzorov, A. Avishai, B. P. Rand, Use of an underlayer for large area crystallization

of rubrene thin films, Chemistry of Materials 29 (16) (2017) 6666–6673 (2017). doi:10.1021/acs.chemmater.7b01143.

[23] T. R. Fielitz, R. J. Holmes, Crystal morphology and growth in annealed rubrene thin films, Crystal Growth & Design 16 (8) (2016) 4720–4726 (2016). doi:10.1021/acs.cgd.6b00783.

[24] K. Abbasi, D. Wang, M. A. Fusella, B. P. Rand, A. Avishai, Methods for conducting electron backscattered diffraction (EBSD) on polycrystalline organic molecular thin films, Microscopy and Microanalysis 24 (4) (2018) 420—-423 (2018). doi:10.1017/S1431927618000442.

[25] J. Stöhr, NEXAFS spectroscopy, Vol. 25, Springer Science & Business Media, 2013 (2013).

[26] A. Smith, H. Ade, Quantitative orientational analysis of a polymeric material (Kevlar® fibers) with x-ray microspectroscopy, Applied Physics Letters 69 (25) (1996) 3833–3835 (1996). doi:10.1063/1.117120.

[27] B. Bräuer, A. Virkar, S. C. Mannsfeld, D. P. Bernstein, R. Kukreja, K. W. Chou, T. Tyliszczak, Z. Bao, Y. Acremann, X-ray microscopy imaging of the grain orientation in a pentacene field-effect transistor, Chemistry of Materials 22 (12) (2010) 3693–3697 (2010). doi:10.1021/cm100487j.

[28] B. Watts, T. Schuettfort, C. R. McNeill, Mapping of domain orientation and molecular order in polycrystalline semiconducting polymer films with soft x-ray microscopy, Advanced Functional Materials 21 (6) (2011) 1122–1131 (2011). doi:10.1002/adfm.201001918.

[29] A. L. Foggiatto, H. Suga, Y. Takeichi, K. Ono, Y. Takahashi, K. Kutsukake, T. Ueba, S. Kera, T. Sakurai, Dependence of substrate work function on the energy-level alignment at organic–organic heterojunction interface, Japanese Journal of Applied Physics 58 (SB) (2019) SBBG06 (feb 2019). doi:10.7567/1347-4065/aaffbf.

[30] Y. Takeichi, N. Inami, H. Suga, C. Miyamoto, T. Ueno, K. Mase, Y. Takahashi, K. Ono, Design and performance of a compact scanning transmission x-ray microscope at the photon factory, Review of Scientific Instruments 87 (1) (2016) 013704 (2016). doi:10.1063/1.4940409.

[31] D. Käfer, L. Ruppel, G. Witte, C. Wöll, Role of molecular conformations in rubrene thin film growth, Physical Review Letters 95 (16) (2005) 166602 (2005). doi:10.1103/PhysRevLett.95.166602.

[32] T. Mukherjee, S. Sinha, M. Mukherjee, Electronic structure of twisted and planar rubrene molecule: A density functional study, Physical Chemistry Chemical Physics 20 (2018) 18623–18629 (2018). doi:10.1039/c8cp02318b.